Chemical Science

ROYAL SOCIETY OF CHEMISTRY

EDGE ARTICLE

View Article Online
View Journal | View Issue

Check for updates

Cite this: *Chem. Sci.*, 2025, **16**, 12587

All publication charges for this article have been paid for by the Royal Society of Chemistry

Modulation of the electronic structure of nickel selenide *via* iron doping for energy-saving hydrogen production coupled with sulfion upgradation†

Shuixiang Xie,‡[a] Xiaojun Wang,‡[a] Yuhuan Li,[a] Shijie Liu,[a] Jiahui Qian,[a] Yuhan Zhang,[a] Linling Jiang,[a] Zhe Cao,[a] Zhenhao Yan,[a] Xiaoyu Wan,[a] Zhaohang Yang,[a] Longhua Zou,*[b] Wei Zhang*[a] and Rui-Qing Li *[a]

Hybrid water electrolysis is a promising approach for energy-saving hydrogen (H_2) generation by replacing the oxygen evolution reaction with the thermodynamically advantageous sulfion oxidation reaction (SOR). Herein, we designed iron-modified nickel selenide nanosheet arrays (Fe-$Ni_{0.85}Se$) and used them as an electrocatalyst in bifunctional hydrogen evolution reaction (HER) and SOR to simultaneously facilitate H_2 production and sulfion conversion into a valuable sulfur product. Fe-$Ni_{0.85}Se$ requires a low overpotential of 114 mV for the HER and a working potential of 0.340 V for the anodic SOR to attain 10 mA cm^{-2}. Moreover, the two-electrode hybrid electrolysis cell employing Fe-$Ni_{0.85}Se$ as the cathode and anode requires a small voltage of 0.439 V at 10 mA cm^{-2}, which greatly reduces the operating voltage by 1.186 V compared with that for overall water splitting, realizing energy-saving H_2 production and high-value-added sulfur production. Theoretical calculations prove that Fe modification can accelerate water dissociation, optimize the adsorption behavior of hydrogen adsorption and sulfion, and promote the conversion process of sulfur intermediates. This study offers a simple approach to develop bifunctional catalytic electrodes for economically viable H_2 generation and sulfur recovery.

Received 10th March 2025
Accepted 28th May 2025

DOI: 10.1039/d5sc01884f

rsc.li/chemical-science

Open Access Article. Published on 29 maj 2025. Downloaded on 2026-02-19 00:00:16.
This article is licensed under a Creative Commons Attribution-NonCommercial 3.0 Unported Licence.

Introduction

Fossil fuel consumption and environmental deterioration have increased the demand for sustainable and clean energy sources.[1,2] As a leading clean energy source, hydrogen (H_2) possesses the advantages of high energy density and environmental benignness, which are crucial for future energy transitions.[3] Traditional H_2 production methods face many problems, such as serious environmental pollution, complicated equipment processes and large investment/operational expenses. In comparison, electrocatalytic overall water splitting (OWS) powered by renewable energy is a promising technology to generate high-purity H_2 because of its mild operating conditions and simplicity.[4,5] However, this technology suffers from high voltages and electricity expenses owing to the presence of the sluggish oxygen evolution reaction (OER) at the anode, which results in increased energy consumption.[6,7] At present, precious-metal-based materials including Pt/C, RuO_2 and IrO_2 are excellent materials used to lower energy expenditure, but their low reserves and high costs hinder their commercialization.[8–10] Therefore, it is appealing to exploit high-efficiency electrocatalytic systems and inexpensive catalysts.

Currently, researchers have adopted hybrid water electrolysis (HWE) by employing the thermodynamically favorable oxidation reactions of small molecules, including methanol, glycerol, urea, 5-hydroxymethylfurfural (HMF), and hydrazine, as substitutes for the OER at the anode, leading to optimized catalytic systems and reduced energy consumption.[11–13] Wang *et al.* prepared oxygen-vacancy-rich Co_3O_4 and coupled the catalytic oxidation of HMF with the hydrogen evolution reaction (HER) to produce FDCA and H_2 at low voltages.[14] Similarly, Duan *et al.* reported the Au/CoOOH catalyst, which catalytically converted benzyl alcohol into high-value-added products while realizing energy-saving H_2 production.[15] Among these alternative reactions, the sulfion oxidation reaction (SOR; $S^{2-} = S + 2e^-$, −0.48 V *vs.* RHE) has the thermodynamic advantage.[16,17] Meanwhile, toxic sulfion-containing wastewater is common in many industrial processes and has adverse effects on human health and the ecological environment. Therefore, combining the SOR with the HER can simultaneously achieve low-voltage H_2 generation and the degradation/conversion of

[a]*School of Textile and Clothing, Nantong University, Nantong 226019, PR China. E-mail: liruiqing@ntu.edu.cn; zhangwei@ntu.edu.cn*

[b]*College of Food and Biological Engineering, Chengdu University, Chengdu 610106, China. E-mail: zoulonghua@cdu.edu.cn*

† Electronic supplementary information (ESI) available. See DOI: https://doi.org/10.1039/d5sc01884f

‡ These authors contributed equally to this work.

© 2025 The Author(s). Published by the Royal Society of Chemistry

Open Access Article. Published on 29 maj 2025. Downloaded on 2026-02-19 00:00:16.
This article is licensed under a Creative Commons Attribution-NonCommercial 3.0 Unported Licence.

sulfur-rich sewage to value-added sulfur without adding other oxidants.[18,19]

As we know, the formation and conversion of polysulfide intermediates are accompanied by a 16-electron transfer process during the SOR, resulting in slow catalytic kinetics.[20,21] Meanwhile, sulfur species can easily poison metallic catalysts, greatly reducing their activities and stabilities. To resolve these challenges, researchers have engaged diverse strategies such as heteroatom doping and heterostructure construction to regulate electronic structures and reduce reaction energy barriers for realizing high catalytic performances.[22–25] However, most prepared catalysts display monofunctional catalytic performances for either the SOR or the HER, which can lead to the incompatibility and deterioration of catalysts and high preparation costs when pairing them in an electrolytic cell. Therefore, relevant studies on bifunctional catalysts for the HER and SOR to achieve H_2 production are of great significance.

Herein, we developed hierarchical and efficient bimetallic selenide (Fe-$Ni_{0.85}Se$) nanosheet arrays, which serve as a bifunctional catalyst to catalyze H_2 production and sulfion ion oxidation. As expected, Fe-$Ni_{0.85}Se$ displays remarkable catalytic activities for the HER and SOR. The combined Fe-$Ni_{0.85}Se$–based hybrid water electrolyzer possesses good catalytic activity and durability and needs a low cell voltage of 0.439 V at 10 mA cm^{-2}, achieving energy-efficiency H_2 production and sulfion upgradation to valuable sulfur. The outstanding catalytic performances of Fe-$Ni_{0.85}Se$ are attributed to the regulation of the composition and electronic structure, which promotes catalytic intermediate adsorption and decreases the energy barriers of catalytic reactions.

Results and discussion

Synthesis and characterization

The preparation scheme for Fe-$Ni_{0.85}Se$ is displayed in Fig. 1a. Initially, the hydrothermal process was adopted to synthesize NiFe layered double hydroxide (NiFe LDH) on a nickel foam (NF) substrate, and the corresponding phase was confirmed by X-ray diffraction (XRD; Fig. S1†). The scanning electron microscopy (SEM) images show the uniform and interconnected growth of NiFe LDH nanosheets with a relatively smooth surface on the NF (Fig. 1b and c). Subsequently, black $Ni_{0.85}Se$ and Fe-$Ni_{0.85}Se$ products were obtained by a hydrothermal selenization process. The several typical diffraction peaks at 33.1°, 44.6°, 50.5°, 59.9°, 61.7° and 69.6° can be attributed to the (101), (102), (110), (103), (201) and (202) lattice planes of hexagonal $Ni_{0.85}Se$ (JCPDS No. 18-0888), respectively, confirming the synthesis of $Ni_{0.85}Se$ and Fe-$Ni_{0.85}Se$ (Fig. 1d). Although Fe-$Ni_{0.85}Se$ maintains a similar nanosheet-like morphology (Fig. 1e and S2†), careful observation shows that the Fe-$Ni_{0.85}Se$ nanosheets are composed of many nanoparticles with diameters of about 100 nm, which is beneficial for exposing abundant active sites and promoting rapid mass transport. Transmission electron microscopy (TEM) was performed to identify the morphology of Fe-$Ni_{0.85}Se$, which further confirms its nanosheet structure composed of nanoparticles (Fig. 1f). In the high-resolution TEM (HRTEM) image (Fig. 1g), the interplanar spacing of 0.268 nm is attributed to the (101) crystal plane of Fe-$Ni_{0.85}Se$. The elemental mapping images (Fig. 1h–k) reveal the presence of Ni, Fe and Se elements, which are uniformly distributed on the surface of Fe-$Ni_{0.85}Se$ nanosheets.

X-ray photoelectron spectroscopy (XPS) tests were carried out to detect surface chemical states. In Fig. 2a, the survey XPS spectrum confirms the coexistence of Ni, Fe and Se elements in the Fe-$Ni_{0.85}Se$ sample. Fig. 2b displays the high-resolution Ni 2p spectrum of Fe-$Ni_{0.85}Se$, and the two peaks located at 852.5 and 869.9 eV belong to the Ni $2p_{3/2}$ and Ni $2p_{1/2}$ of Ni^{2+}, and the binding energies at 855.5 and 873.1 eV are indexed to the Ni $2p_{3/2}$ and Ni $2p_{1/2}$ of Ni^{3+}, respectively.[26] The remaining two peaks at 861.1 and 879.4 eV are ascribed to satellite peaks. Similarly, the Fe 2p spectrum (Fig. 2c) shows three pairs of $2p_{3/2}/2p_{1/2}$ doublet peaks located at 707.8/721.5, 712.0/725.3 and 716.6/729.7 eV.[27] For Se species, the Se 3d spectrum of Fe-$Ni_{0.85}Se$ (Fig. 2d) is deconvoluted into two peaks at 53.7 and 54.8 eV, which are attributed to Se $3d_{5/2}$ and Se $3d_{3/2}$, respectively, indicating the presence of the metal–Se bond. The peak at 58.5 eV is attributed to the Se–O bond, ascribed to the unavoidable slight surface oxidation.[28]

Electrochemical performances

The HER performance of Fe-$Ni_{0.85}Se$ was assessed in a three-electrode system. In Fig. 3a and g, Fe-$Ni_{0.85}Se$ displays excellent HER activity and requires small overpotentials of 114 and 365 mV to deliver current densities of 10 and 400 mA cm^{-2}, lower than those of $Ni_{0.85}Se$ (138 and 411 mV), respectively, confirming the crucial role of Fe introduction in improving catalytic performance of $Ni_{0.85}Se$. The catalytic activity of Fe-$Ni_{0.85}Se$ also surpasses that of many developed HER catalysts (Fig. 3d and Table S1†).

Tafel plots were fitted from the corresponding polarization curves to investigate HER kinetics. Fe-$Ni_{0.85}Se$ possesses a small Tafel slope of 71 mV dec^{-1} (Fig. 3b and g), smaller than that of $Ni_{0.85}Se$ (93 mV dec^{-1}), implying that the HER process of Fe-$Ni_{0.85}Se$ follows a Volmer–Heyrovsky pathway. The low Tafel slope of Fe-$Ni_{0.85}Se$ suggests that it has quick HER kinetics and outstanding catalytic activities because of the electronic structure optimization of $Ni_{0.85}Se$ after Fe doping.[29,30] To deeply understand the origin of the high intrinsic activities of Fe-$Ni_{0.85}Se$, electrochemical impedance spectroscopy (EIS) was performed. In Fig. 3c and g, the Nyquist plots show that Fe-$Ni_{0.85}Se$ has a smaller charge-transfer resistance (R_{ct}; 0.5 Ω) than $Ni_{0.85}Se$ (0.6 Ω), implying the key role of Fe doping in promoting the charge transfer rate. Furthermore, the number of catalytic sites on Fe-$Ni_{0.85}Se$ can be quantified using the electrochemically active surface area (ECSA) derived from the electrochemical double-layer capacitance (C_{dl}), which is calculated from cyclic voltammograms (Fig. S3†). In Fig. 3e and g, the calculated C_{dl} and ECSA values of Fe-$Ni_{0.85}Se$ (17.7 mF cm^{-2} and 442.5 cm^{-2}) are higher than those of $Ni_{0.85}Se$ (15.1 mF cm^{-2} and 377.5 cm^{-2}), indicating that Fe-$Ni_{0.85}Se$ has more catalytic sites than $Ni_{0.85}Se$, in agreement with the remarkable activity of Fe-$Ni_{0.85}Se$.[31] In Fig. 3f, the ECSA-normalized curves further reveal that Fe-$Ni_{0.85}Se$ still has higher catalytic performances than

© 2025 The Author(s). Published by the Royal Society of Chemistry

Open Access Article. Published on 29 maj 2025. Downloaded on 2026-02-19 00:00:16.
This article is licensed under a Creative Commons Attribution-NonCommercial 3.0 Unported Licence.

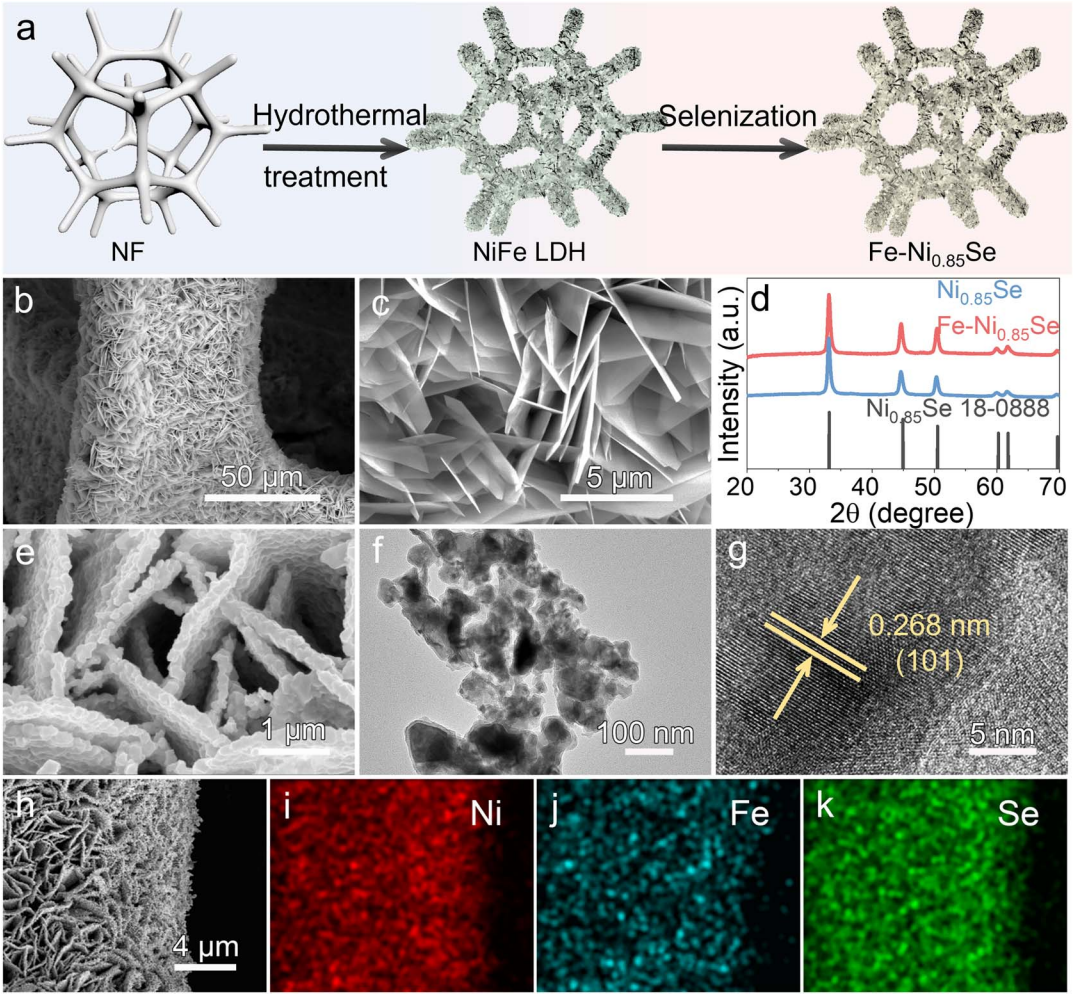

Fig. 1 (a) Schematic of preparation of *x*Fe-$Ni_{0.85}Se$. (b and c) SEM images of NiFe LDH nanosheets. (d) XRD patterns, (e) SEM, (f) TEM, (g) HRTEM, (h–k) SEM and homologous element mapping images of Fe-$Ni_{0.85}Se$.

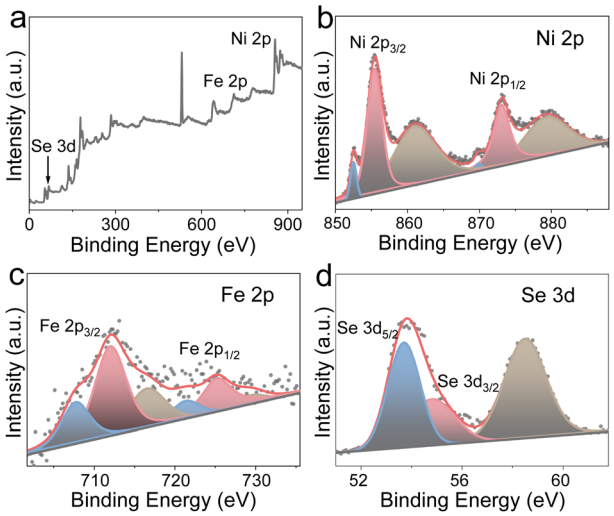

Fig. 2 (a) Survey XPS, (b) Ni 2p, (c) Fe 2p and (d) Se 3d spectra of Fe-$Ni_{0.85}Se$.

$Ni_{0.85}Se$, indicating that Fe doping can effectively improve the intrinsic activity of $Ni_{0.85}Se$ and expose more catalytic sites. Furthermore, long-term stability is a key parameter for catalysts. In Fig. 3h, the chronopotentiometry (*v*–*t*) curve displays that Fe-$Ni_{0.85}Se$ has outstanding durability with almost-unchanged potentials during a 50-h test. Moreover, the nanosheet-like morphology of Fe-$Ni_{0.85}Se$ does not change greatly (Fig. S4†), and the Ni, Fe and Se elements are homogeneously distributed on the surface of Fe-$Ni_{0.85}Se$ nanosheets (Fig. S5†), indicating their outstanding structural stability.

The OER performance of Fe-$Ni_{0.85}Se$ was further measured. In Fig. 4a, Fe-$Ni_{0.85}Se$ displays good OER activities and requires low potentials of 1.485 and 1.577 mV to deliver 50 and 400 mA cm^{-2}, much lower than those required by $Ni_{0.85}Se$ (1.536 and 1.694 mV) and RuO_2 (1.538 and 1.786 mV), respectively. Even so, the OER potentials for Fe-$Ni_{0.85}Se$ are still high, leading to high energy consumption when coupled with the HER. Therefore, it is promising to replace the OER with the SOR to lower the anode potential and achieve energy-efficient H_2 production. The SOR activities were evaluated in 1 M NaOH containing different concentrations of Na_2S (0.5–1.5 M). The SOR activity of Fe-

Open Access Article. Published on 29 maj 2025. Downloaded on 2026-02-19 00:00:16.
This article is licensed under a Creative Commons Attribution-NonCommercial 3.0 Unported Licence.

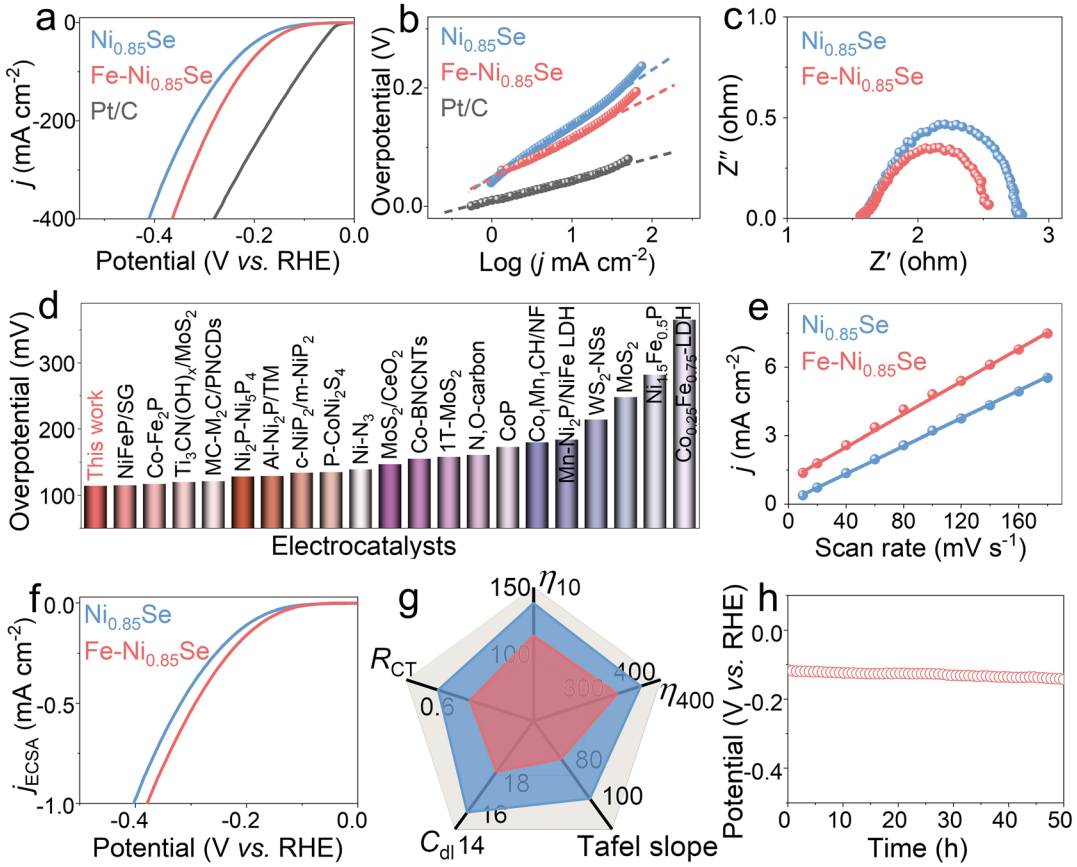

Fig. 3 (a) HER polarization curves and (b) corresponding Tafel slopes of various catalysts. Comparison of (c) EIS plots and (d) overpotentials of recently developed catalysts and Fe-$Ni_{0.85}Se$. (e) C_{dl} values and (f) ECSA-normalized polarization curves of $Ni_{0.85}Se$ and Fe-$Ni_{0.85}Se$. (g) HER performance radar chart. (h) Durability test of Fe-$Ni_{0.85}Se$.

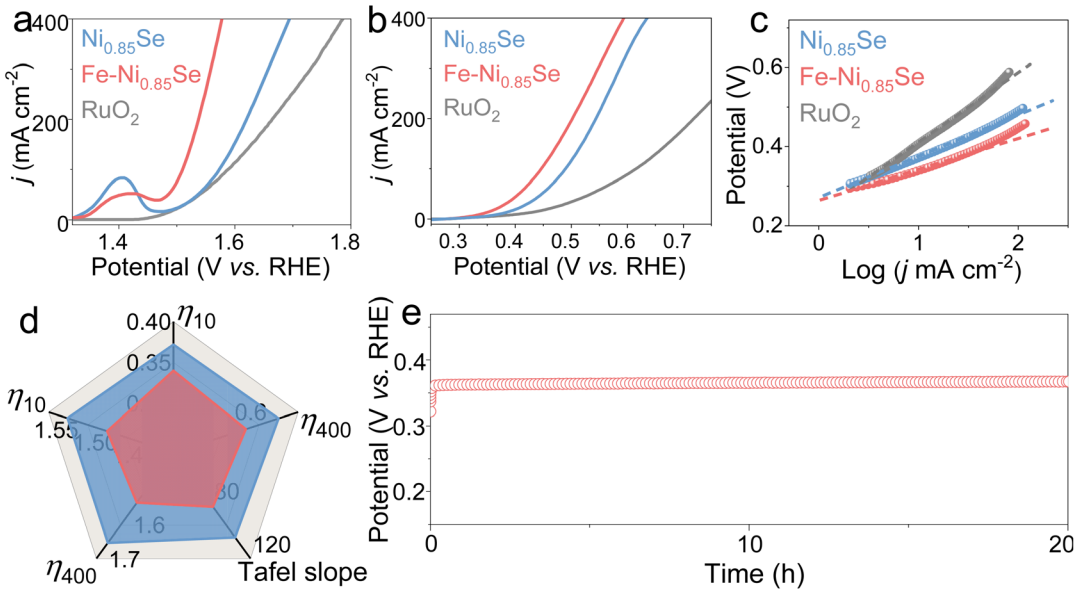

Fig. 4 Polarization curves of the (a) OER and (b) SOR and (c) Tafel slopes of the catalysts. (d) OER and SOR performance radar chart of $Ni_{0.85}Se$ and Fe-$Ni_{0.85}Se$. (e) Stability measurement of Fe-$Ni_{0.85}Se$.

© 2025 The Author(s). Published by the Royal Society of Chemistry

Open Access Article. Published on 29 maj 2025. Downloaded on 2026-02-19 00:00:16.
This article is licensed under a Creative Commons Attribution-NonCommercial 3.0 Unported Licence.

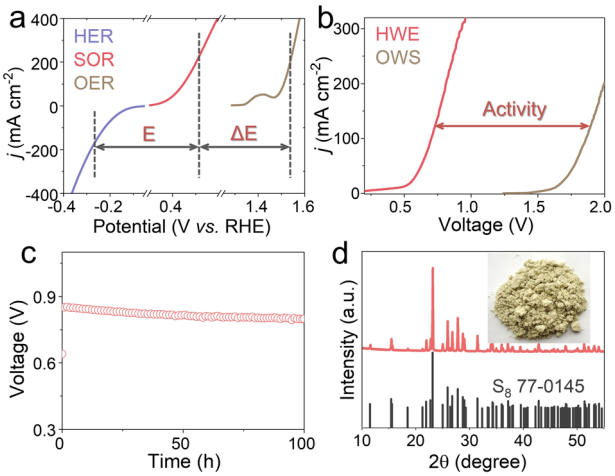

Fig. 5 (a) Voltage difference between the HER and SOR/OER. (b) Polarization curves of HWE and OWS systems for Fe-$Ni_{0.85}Se$. (c) Durability test of the HWE process. (d) XRD pattern of the S product. Inset: Digital image of S.

$Ni_{0.85}Se$ rapidly increases when the concentration of Na_2S increases to 1 M (Fig. S6†). In 1 M NaOH containing 1 M Na_2S, Fe-$Ni_{0.85}Se$ displays splendid SOR activities with low potentials of 0.340 and 0.593 V at 10 and 400 mA cm^{-2} (Fig. 4b and d), smaller than those of $Ni_{0.85}Se$ (0.372 and 0.635 V), RuO_2 (0.406 and 0.893 V) and most previously developed SOR materials (Table S2†), respectively. Moreover, the SOR process on Fe-$Ni_{0.85}Se$ shows greatly reduced potentials compared with the OER, confirming the feasibility of replacing the OER with the SOR to realize low cell voltages. The corresponding Tafel plots (Fig. 4c) manifest that Fe-$Ni_{0.85}Se$ still possesses a smaller Tafel slope value (81 mV dec^{-1}) than $Ni_{0.85}Se$ (104 mV dec^{-1}) and RuO_2 (179 mV dec^{-1}), implying that Fe-$Ni_{0.85}Se$ has fast SOR kinetics.[32] The stability of Fe-$Ni_{0.85}Se$ was also studied. In Fig. 4e, Fe-$Ni_{0.85}Se$ exhibits almost-constant potentials over a 20-h test, and the corresponding nanosheet-like morphology (Fig. S7†) and homogeneous distribution of Ni, Fe and Se elements are well maintained (Fig. S8†), further illustrating its good durability for the SOR.

Motivated by the eminent HER and SOR performances of Fe-$Ni_{0.85}Se$ (Fig. 5a), traditional and hybrid two-electrode electrolyzers were assembled. In Fig. 5b, the HWE electrolyzer can output current densities of 10 and 200 mA cm^{-2} at low cell voltages (V_{10} and V_{200}) of 0.439 and 0.811 V, respectively, lower than those needed in the conventional OWS system (1.625 and 1.998 V). In Fig. 5c, the stability test curve shows that Fe-$Ni_{0.85}Se$ operates steadily for 100 h with negligible voltage degradation, confirming its outstanding durability. After the durability test, the relevant electrolyte was acidified with sulfuric acid, and yellow powders were obtained, which are verified to be elemental sulfur (S_8, PDF#77-0145, Fig. 5d), implying high valuable sulfur recovery. These results indicate that the substitution of the OER by the SOR not only significantly decreases

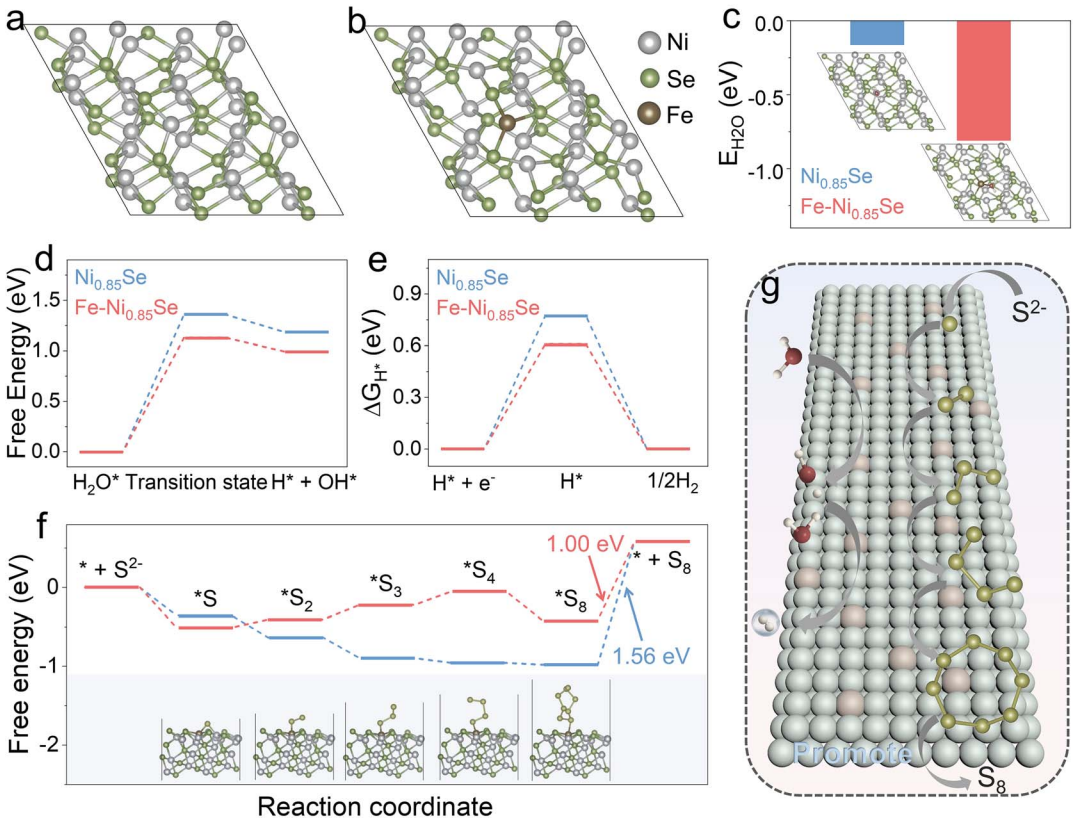

Fig. 6 Structural models of (a) $Ni_{0.85}Se$ and (b) Fe-$Ni_{0.85}Se$. (c) Water adsorption, (d) activation energy, (e) ΔG_{H^*} comparison, and (f) free energy profiles of the stepwise SOR of $Ni_{0.85}Se$ and Fe-$Ni_{0.85}Se$. (g) Schematic of the HER and SOR processes.

Open Access Article. Published on 29 maj 2025. Downloaded on 2026-02-19 00:00:16.
This article is licensed under a Creative Commons Attribution-NonCommercial 3.0 Unported Licence.

the cell voltages of H_2 production but also affords a high-value sulfur product in sulfion-rich wastewater.

Theoretical analysis

To reveal the origin of the high HER and SOR performances of Fe-$Ni_{0.85}Se$, we carried out density functional theory (DFT) simulations to illustrate its reaction mechanism. The structure models are displayed in Fig. 6a and S9†. The adsorption and dissociation of H_2O and free energy change of H* (ΔG_{H^*}) for the HER were analyzed. In Fig. 6b, Fe-$Ni_{0.85}Se$ shows a lower H_2O adsorption energy (E_{H_2O}; −0.81 eV) than $Ni_{0.85}Se$ (−0.16 eV), indicating that H_2O molecules are easily adsorbed on the surface of Fe-$Ni_{0.85}Se$ for the subsequent dissociation process.[33] For $Ni_{0.85}Se$, the H_2O dissociation and adsorbed hydrogen (H*) generation energy barriers are calculated to 1.36 and 1.18 eV, respectively. After Fe doping, the corresponding energy barriers of Fe-$Ni_{0.85}Se$ decrease to 1.13 and 0.99 eV, respectively, indicating that the H_2O dissociation process of Fe-$Ni_{0.85}Se$ is more thermodynamically favorable to produce H* than $Ni_{0.85}Se$.[34] Meanwhile, the ΔG_{H^*} value of Fe-$Ni_{0.85}Se$ is calculated to be 0.61 eV (Fig. 6e), which is close to thermoneutrality compared with that of $Ni_{0.85}Se$ (0.77 eV), indicating the fast H_2 production capacity of Fe-$Ni_{0.85}Se$.[35] The structure models of H_2O dissociation and H* on $Ni_{0.85}Se$ and Fe-$Ni_{0.85}Se$ are displayed in Fig. S10–12†. Additionally, DFT analysis of the SOR process was carried out, and the intermediate energy changes of the stepwise oxidation of S^{2-} to S_8 ($S^{2-} \rightarrow S^* \rightarrow S_2^* \rightarrow S_3^* \rightarrow S_4^* \rightarrow S_8^* \rightarrow S_8$) on $Ni_{0.85}Se$ and Fe-$Ni_{0.85}Se$ were estimated on $Ni_{0.85}Se$ and Fe-$Ni_{0.85}Se$ (Fig. 6f and S13†). Notably, Fe-$Ni_{0.85}Se$ has a more negative energy barrier value for S^{2-} adsorption (ΔG_{*S}, −0.51 eV) than $Ni_{0.85}Se$ (−0.36 eV), implying the favorable S^{2-} adsorption for Fe-$Ni_{0.85}Se$, which is vital for the subsequent desulfurization process.[36,37] According to calculated free energy changes (Fig. 6f), the desorption process from $*S_8$ to S_8 is identified as the rate-determining step (RDS) for $Ni_{0.85}Se$, requiring a high energy barrier of 1.56 eV. After Fe doping, Fe-$Ni_{0.85}Se$ has a low free energy barrier of 1.00 eV for desorbing $*S_8$ to S_8, which effectively increases SOR performances. These results indicate that Fe introduction not only promotes water dissociation and optimizes the thermodynamic efficiency of H* during the HER but also speeds up the oxidation process of S^{2-} for the SOR, consistent with the above-discussed high HER and SOR performances of Fe-$Ni_{0.85}Se$.

Conclusions

In summary, we constructed an Fe-$Ni_{0.85}Se$ catalyst *via* hydrothermal and selenization strategies, which exhibited splendid catalytic activities towards the HER and SOR in an alkaline electrolyte due to the synergistic effect of Fe incorporation and uniform nanosheet arrays. The resultant Fe-$Ni_{0.85}Se$ realizes the 10 mA cm^{-2} at a low overpotential of 114 mV for the HER and a potential of 0.340 V for the SOR. Meanwhile, the assembled Fe-$Ni_{0.85}Se$–based electrolyzer achieves energy-saving H_2 generation and sulfion upgradation to a value-added sulfur product, which needs low cell voltages of 0.439 and 0.811 V to reach 10 and 200 mA cm^{-2}. DFT calculations reveal that Fe incorporation plays vital roles in increasing HER and SOR performances, which can enhance the adsorption of catalytic reactants and intermediates and lower energy barriers for the HER and SOR. This study offers a new scheme for the efficient preparation of H_2 and sulfur in sulfion-containing wastewater.

Data availability

The relevant experimental and characterization data are available in the article and the ESI.†

Author contributions

Shuixiang Xie: data curation and formal analysis. Xiaojun Wang: data curation and formal analysis. Yuhuan Li: investigation. Shijie Liu: formal analysis. Jiahui Qian: investigation. Yuhan Zhang: data curation. Linling Jiang: data curation. Zhe Cao: formal analysis. Zhenhao Yan: investigation. Xiaoyu Wan: writing-review and editing. Zhaohang Yang: investigation. Longhua Zou: software. Wei Zhang: conceptualization, writing-review and editing. Rui-Qing Li: conceptualization, writing-review and editing.

Conflicts of interest

There are no conflicts to declare.

Acknowledgements

This work was financially supported by the National Natural Science Foundation of China (No. 22302103), the Natural Science Foundation of Jiangsu Province (No. BK20230619), the Natural Science Foundation of the Jiangsu Higher Education Institutions of China (No. 23KJB540003), the Natural Science Foundation of Nantong Municipality (No. JC2023015), the Opening Project of Key Laboratory of Advanced Electrode Materials for Novel Solar Cells for Petroleum and Chemical Industry of China, Suzhou University of Science and Technology (No. 2024A038), the Postgraduate Research & Practice Innovation Program of Jiangsu Province (No. KYCX25_3762), the College Students Innovation and Entrepreneurship Training Program, and the Large Instruments Open Foundation of Nantong University (No. KFJN2457). The authors also thank Ceshigo Research Service (https://www.ceshigo.com) for theoretical calculation and the Nantong University Analysis and Testing Center for technical support.

Notes and references

1 J. Turner, *Science*, 2022, **376**, 1361.
2 P. Shi, J. Li, Y. Song, N. Xu and J. Zhu, *Nano Lett.*, 2024, **24**, 5673.
3 X. Zhou, J. Zhang, M. Zhang, X. Du, W. Bao, J. Han, X. Lin, P. Zhang and Z. Luo, *Inorg. Chem. Front.*, 2025, **12**, DOI: 10.1039/D5QI00418G.

© 2025 The Author(s). Published by the Royal Society of Chemistry

Open Access Article. Published on 29 maj 2025. Downloaded on 2026-02-19 00:00:16.
This article is licensed under a Creative Commons Attribution-NonCommercial 3.0 Unported Licence.

4 Y. Wu, M. Chen, H. Sun, T. Zhou, X. Chen, G. Na, G. Qiu, D. Li, N. Yang, H. Zheng, Y. Chen, B. Wang, J. Zhao, Y. Zhang, J. Zhang, F. Liu, H. Cui, T. He and Q. Liu, *Appl. Catal. B*, 2025, **360**, 124548.
5 X. Deng, X. Zheng, Z. Gong, W. Tan and X. Pei, *Chin. J. Rare Met.*, 2023, **47**, 43.
6 R. Li, S. Guo, X. Wang, X. Wan, S. Xie, Y. Liu, C. Wang, G. Zhang, J. Cao, J. Dai, M. Ge and W. Zhang, *Chem. Sci.*, 2024, **15**, 10084.
7 C. Walter, P. Menezes and M. Driess, *Chem. Sci.*, 2021, **12**, 8603.
8 Y. Wu, M. Chen, D. Liu, H. Sun, T. Zhou, G. Na, G. Qiu, D. Li, Y. Chen, J. Zhao, Y. Zhang, J. Zhang, H. Pan, F. Liu, H. Cui and Q. Liu, *J. Mater. Sci. Technol.*, 2025, **215**, 111.
9 Y. Wang, S. Wang, Z. Ma, L. Yan, X. Zhao, Y. Xue, J. Huo, X. Yuan, S. Li and Q. Zhai, *Adv. Mater.*, 2022, **34**, 2107488.
10 D. Li, M. Chen, D. Liu, C. Shen, H. Sun, Y. Zhang, T. He, Q. Lu, B. Li, T. Zhou, B. Wang, Y. Wu, G. Na, Y. Chen, J. Zhao, Y. Zhang, J. Zhang, F. Liu, H. Cui and Q. Liu, *Adv. Energy Mater.*, 2024, **15**, 2404714.
11 P. Zhu, M. Shi, Z. Shen, X. Liao and Y. Chen, *Chem. Sci.*, 2024, **15**, 4723.
12 P. Zhou, X. Lv, S. Tao, J. Wu, H. Wang, X. Wei, T. Wang, B. Zhou, Y. Lu, T. Frauenheim, X. Fu, S. Wang and Y. Zou, *Adv. Mater.*, 2022, **34**, 2204089.
13 R. Li, S. Zeng, B. Sang, C. Xue, K. Qu, Y. Zhang, W. Zhang, G. Zhang, X. Liu, J. Deng, O. Fontaine and Y. Zhu, *Nano Res.*, 2023, **16**, 2543.
14 Y. Lu, T. Liu, C. Dong, C. Yang, L. Zhou, Y. Huang, Y. Li, B. Zhou, Y. Zou and S. Wang, *Adv. Mater.*, 2022, **34**, 2107185.
15 Z. Li, Y. Yan, S. Xu, H. Zhou, M. Xu, L. Ma, M. Shao, X. Kong, B. Wang, L. Zheng and H. Duan, *Nat. Commun.*, 2022, **13**, 147.
16 L. Zhang, Z. Wang and J. Qiu, *Adv. Mater.*, 2022, **34**, 2109321.
17 W. Wang, Q. Mao, S. Jiang, K. Deng, H. Yu, Z. Wang, Y. Xu, L. Wang and H. Wang, *Appl. Catal., B*, 2024, **340**, 123194.
18 R. Li, X. Wang, S. Xie, S. Guo, Z. Cao, Z. Yan, W. Zhang and X. Wan, *Chem. Sci.*, 2025, **16**, 809.
19 H. Wang, H. Yao, Q. Guo and H. Xia, *J. Nanjing Univ. Nat. Sci. Ed.*, 2024, **23**, 45.
20 L. Yi, Y. Ji, P. Shao, J. Chen, J. Li, H. Li, K. Chen, X. Peng and Z. Wen, *Angew. Chem., Int. Ed.*, 2021, **60**, 21550.
21 Y. Pei, D. Li, C. Qiu, L. Yan, Z. Li, Z. Yu, W. Fang, Y. Lu and B. Zhang, *Angew. Chem., Int. Ed.*, 2024, **63**, e202411977.
22 R. Li, X. Xu, J. Zeng, X. Zhang, X. Wan, S. Guo, X. Wang, S. Xie, Z. Cao, Y. Zhang, C. Wang, J. Deng, O. Fontaine, M. Ge, J. Dai, G. Zhang, W. Zhang, X. Wang and Y. Zhu, *Nano Lett.*, 2025, **25**, 1272.
23 R. Xu and Z. Wang, *J. Nantong Univ., Nat. Sci. Ed.*, 2024, **23**, 21.
24 T. Xue, Z. Huang, H. Gu and H. Zhang, *Chin. J. Rare Met.*, 2024, **48**, 90.
25 R. Li, H. Su, S. Xie, X. Wan, C. Wang, G. Zhang, M. Ge, J. Dai, C. Xue, C. Li, J. Cao and W. Zhang, *Rare Met*, 2024, **43**, 6426.
26 H. Yan, Y. Xie, A. Wu, Z. Cai, L. Wang, C. Tian, X. Zhang and H. Fu, *Adv. Mater.*, 2019, **31**, 1901174.
27 C. Lyu, Y. Li, J. Cheng, Y. Yang, K. Wu, J. Wu, H. Wang, W. Lau, Z. Tian, N. Wang and J. Zheng, *Small*, 2023, **19**, 2302055.
28 Y. Chang, P. Zhai, J. Hou, J. Zhao and J. Gao, *Adv. Energy Mater.*, 2022, **12**, 2102359.
29 X. Du, J. Zhang, X. Zhou, M. Zhang, N. Wang, X. Lin, P. Zhang and Z. Luo, *Green Chem.*, 2025, **27**, 3515.
30 H. Luo, L. Li, F. Lin, Q. Zhang, K. Wang, D. Wang, L. Gu, M. Luo, F. Lv and S. Guo, *Adv. Mater.*, 2024, **36**, 2403674.
31 H. Ding, C. Su, J. Wu, H. Lv, Y. Tan, X. Tai, W. Wang, T. Zhou, Y. Lin, W. Chu, X. Wu, Y. Xie and C. Wu, *J. Am. Chem. Soc.*, 2024, **146**, 7858.
32 H. Yu, W. Wang, Q. Mao, K. Deng, Y. Xu, Z. Wang, X. Li, H. Wang and L. Wang, *J. Mater. Chem. A*, 2023, **11**, 2218.
33 Y. Hu, L. Shao, Z. Jiang, L. Shi, Q. Li, K. Shu, H. Chen, G. Li, Y. Dong, T. Wang, J. Li, L. Jiao and Y. Deng, *Adv. Funct. Mater.*, 2024, **34**, 2411011.
34 Q. Zhou, H. Hu, Z. Chen, X. Ren and D. Ma, *Chem. Sci.*, 2025, **16**, 1597.
35 T. Wang, L. Miao, S. Zheng, H. Qin, X. Cao, L. Yang and L. Jiao, *ACS Catal.*, 2023, **13**, 4091.
36 Y. Pei, D. Li, C. Qiu, L. Yan, Z. Li, Z. Yu, W. Fang, Y. Lu and B. Zhang, *Angew. Chem., Int. Ed.*, 2024, **63**, e202411977.
37 D. He, P. Yang, K. Yang, J. Qiu and Z. Wang, *Adv. Funct. Mater.*, 2024, **34**, 2407601.